Carbon 207 (2023) 207–218

Contents lists available at ScienceDirect

Carbon

journal homepage: www.elsevier.com/locate/carbon

# Controlled doping of carbon catalyst supports by atomic replacement via gasification-assisted heteroatom doping

Felix Herold [a,*], Timo Imhof [b], Paul Roumeliotis [b], Patrick Schühle [c], Marc Ledendecker [d], Magnus Rønning [a,**]

[a] Norwegian University of Science and Technology, Department of Chemical Engineering, Trondheim, 7491, Norway
[b] Technical University of Darmstadt, Department of Chemistry, Ernst-Berl-Institut für Technische und Makromolekulare Chemie, 64287, Darmstadt, Germany
[c] Friedrich-Alexander-Universität Erlangen-Nürnberg, Institute of Chemical Reaction Engineering, 91058, Erlangen, Germany
[d] Technical University Munich, Campus Straubing, Sustainable Energy Materials, Schulgasse 22, 94315, Straubing, Germany

A B S T R A C T

Due to a set of unique properties, carbon materials are applied as supports for metal-based catalysts in a wide variety of established and emerging (electro-)catalytical transformations. By introducing heteroatoms such as N, S and P into carbon supports, metal-support interactions can be tuned, enabling an optimization of catalyst performance in terms of activity, selectivity and stability. However, the exact impact of carbon heteroatom doping on catalyst performance remains often poorly understood, as the effects are inseparable from the clustered influence of other support properties such as texture and nanostructure. In this context, we present gasification-assisted heteroatom doping (GAHD) as a novel, broadly applicable post synthesis approach to exchange carbon surface atoms against heteroatoms while retaining the properties of the parental carbon. Employing GAHD, N, S and P doping of carbons with widely varying properties could be achieved, allowing, for example, incorporation of up to 13.1 wt-% S into an activated carbon at a change of specific surface area of only 4.4%. As a proof-of-concept, comparable N, S and P doped carbon nanofiber supports were used to prepare Pt-based electrocatalysts for the oxygen reduction reaction and probe the influence of the heteroatom dopants on their stability by accelerated stress tests in different potential regimes. In this context, P and S doped supports were found to exhibit a high degree of interaction with Pt, providing increased degradation resistance compared to N and non-doped support.

## 1. Introduction

Due to a tunable, wide space of properties, heteroatom doped carbon materials have been extensively investigated in the fields of energy storage [1,2] and catalysis. In catalysis, they are predominantly applied as catalyst supports for metal nanoparticles or metal single atoms in various high-profile applications, such as proton exchange membrane fuel cells (PEMFC) [3–7], electrochemical $CO_2$ reduction [8], Fischer-Tropsch synthesis [9,10] and various other types of oxidation [11–13] and hydrogenation [14,15] reactions.

Considering the role as catalyst support, there are numerous examples highlighting the opportunities heteroatom doping provides to optimize a catalyst system in terms of activity, selectivity and stability [14,16–19]. In this sense, metal-support interactions can be tailored by heteroatom doping, whereas charge transfer between metal and heteroatom dopant can influence activity and selectivity of a catalyst [9,20–22]. Furthermore, heteroatom doping can improve catalyst stability, by increasing the polarity of the carbon support and enabling coordination of the metal active phase by free electron pairs of the dopant [5,7,14,23–28]. Nevertheless, it has to be emphasized that the precise effects of heteroatom doping on catalyst performance remain often poorly understood, as carbon supported metal catalysts exhibit an extensive number of factors influencing catalytic performance [29–32].

In order to disentangle the effects of heteroatom doping from other support characteristics, a straight-forward approach would be the comparison of series of doped and non-doped carbons, which only differ in the presence or absence of heteroatoms, but not in crystallinity, texture or morphology. However, current synthetic approaches towards heteroatom doped carbons exhibit clear limitations regarding the accessibility of such comparable doped carbon materials. Considering bottom-up synthesis strategies for doped as well as non-doped carbons such as chemical vapor deposition (CVD) as well as pyrolysis, heteroatom doping is usually achieved by exchanging precursors composed of C, H and O with precursors additionally containing N, S or P [33–35]. In this context, the presence of N, S or P in the precursors changes carbon formation pathways fundamentally, thus preventing the synthesis of

* Corresponding author.
** Corresponding author.
*E-mail addresses:* felix.herold@ntnu.no (F. Herold), magnus.ronning@ntnu.no (M. Rønning).

https://doi.org/10.1016/j.carbon.2023.03.023
Received 29 November 2022; Received in revised form 9 March 2023; Accepted 10 March 2023
Available online 10 March 2023

doped and non-doped carbon materials with comparable properties [35]. Post-synthesis doping strategies avoid the complex interplay between heteroatom doping and carbon formation by introducing heteroatoms into an already developed carbon structure, mostly by high-temperature treatment of a carbon material with an impregnated or gaseous heteroatom source [36–40]. However, many post-doping strategies also change the properties of the parental carbon to such an extent that series of comparable doped and non-doped carbons are inaccessible.

Hence, an optimal heteroatom doping method to access comparable doped and non-doped carbons would allow to selectively exchange single carbon atoms against arbitrary heteroatoms, without otherwise disturbing the characteristics of the original carbon. To approach this goal, we propose the novel concept of gasification-assisted heteroatom doping (GAHD). In this method, a gasification agent ($H_2O$, $CO_2$, $H_2$) is utilized to create defects in a carbon material while a simultaneously present gaseous heteroatom source containing N, S or P saturates these newly formed chemisorption sites. Aiming at broad applicability, a minimalistic experimental set-up is used, relying on a gas-washing bottle serving as a simple one-stage saturator for the dosing of the heteroatom source upstream of a tubular furnace. Thus, heteroatom sources utilized in this approach are inexpensive, easy-to-handle liquids, eliminating the need for sophisticated infrastructure for handling and dosing of corrosive, toxic gases (Scheme 1).

Within this contribution, GAHD is studied at the example of N, S and P doping of three typical carbon catalyst support materials which cover a wide range of properties, namely activated carbon (AC), carbon black (CB) and carbon nanofibers (CNF). In order to probe the potential of GAHD to produce heteroatom doped model supports for the examination of the effects of heteroatom doping, Pt nanoparticles are deposited on a series of comparable heteroatom doped CNF with similar N, S and P loading. As a model process, the influence of N, S and P doping of the CNF support on the degradation of PEMFC Pt/C catalysts is examined by subjecting the materials to accelerated stress tests (AST) in two different potential regimes [41,42].

## 2. Materials and methods

### 2.1. Materials

All gases were purchased from Linde AG. 65 wt-% $HNO_3$, 37 wt-% HCl, trimethyl phosphite, carbon disulfide, ethylene diamine and hexachloroplatinic acid (99.95%) were purchased from Sigma Aldrich, while calcium oxalate monohydrate was acquired from Alfa Aesar. Ultrapure water was purchased from VWR, while 70 wt-% $HClO_4$ (ultrapure) and ethanol abs (99.8%) were acquired from Carl Roth. Carbon black (Printex® 85) was provided by Orion Engineered Carbons while activated carbon (Norit A Supra EUR, Cabot) was purchased from Sigma Aldrich. The activated carbon was demineralized (37 wt-% HCl, 90 °C, 24 h) before use, the carbon black was used without further pretreatment.

### 2.2. Preparation of carbon nanofibers

The preparation of platelet carbon nanofibers (CNF) has been described elsewhere [43]. In short, a $Fe_3O_4$ catalyst is reduced in a flow of 100 mL $min^{-1}$ of 25 vol-% $H_2$ in Ar at 600 °C for 6 h in a vertical tubular furnace employing a quartz reactor with a ceramic frit. After flushing with 100 mL $min^{-1}$ Ar for 30 min at 600 °C, carbon nanofibers are grown by CVD for 48 h at 600 °C using a mixture of 50 mL $min^{-1}$ CO and 12.5 mL $min^{-1}$ $H_2$. For purification, the as-grown CNF are dispersed in 65 wt-% $HNO_3$ (ca. 1:14 g $g^{-1}$ CNF/$HNO_3$) at 120 °C for 24 h and subsequently filtrated and washed with deionized water. This purification procedure is carried out three times. Afterwards, the nanofibers are dispersed in 37 wt-% HCl at 90 °C for 24 h, after which they are filtrated, washed with water and dried at 120 °C in static air.

### 2.3. High-temperature hydrogen treatment of CNF

To obtain a carbon surface mostly terminated by H, 500 mg of CNF were heated in a vertical tubular furnace to 950 °C at a heating rate of 10 °C $min^{-1}$ in a stream of 100 mL $min^{-1}$ of $H_2$. After holding 950 °C for 30 °min, the sample was allowed to cool in a flow of 100 mL $min^{-1}$ Ar,

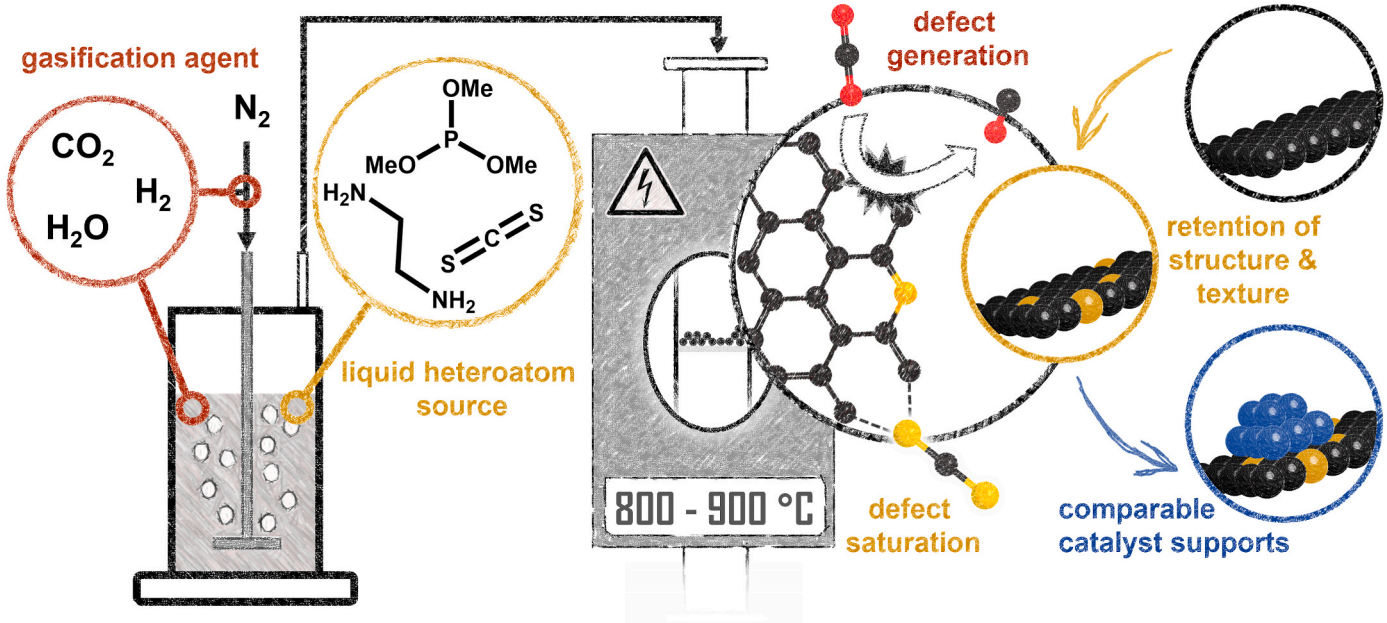


**Scheme 1.** Gasification-assisted heteroatom doping is realized by saturating a gas stream containing a gasification agent with the vapors of a liquid heteroatom source, whereas the gasification agent introduces new surface defects into the carbon lattice, that are subsequently saturated by the heteroatom source. This procedure allows replacement of surface carbon atoms against N, S or P, thus enabling post-synthesis heteroatom doping while retaining carbon properties such as nanostructure and texture.

yielding 470 mg of CNF–H.

### 2.4. Heteroatom doping

Heteroatom doping was conducted in a vertical tubular furnace employing a quartz reactor (ca. 40 mm internal diameter) fitted with a ceramic frit on which the carbon samples were placed. Liquid heteroatom sources were fed as vapors to the reactor by utilizing a gas-washing bottle as saturator upstream of the furnace. The employed gas distribution system controlled by mass flow controllers (MFC, Bronkhorst) allowed to select the flow pathway either through saturator and reactor, or to bypass the saturator and feed gases directly to the furnace during heat-up and cool-down. A flow chart of the employed gas distribution system is provided in Fig. S1. In the following, typical procedures for N, S and P doping are described. The detailed doping procedure of every sample is provided in Tables S1–3 in the SI.

#### 2.4.1. N doping

For N doping, 350 mg of activated carbon, carbon black or carbon nanofibers are placed in the quartz reactor and heated to 875 °C at a rate of 10 °C $min^{-1}$ and 250 mL $min^{-1}$ $N_2$ flow. After reaching the reaction temperature, the gas flow is switched to pass through the saturator containing a mixture of ethylene diamine and water (1:1.5 mol $mol^{-1}$) before entering the furnace. After the desired reaction time, the gas flow is switched to bypass the saturator, and the reactor is allowed to cool. Depending on the parental carbon and the employed reaction time, 300–320 mg of N doped carbon is obtained.

#### 2.4.2. S doping

For S doping, 350 mg of AC, CB or CNF are placed in the quartz reactor and heated to 825 °C for AC and CNF, and 875 °C in case of CB at a rate of 10 °C $min^{-1}$ in an atmosphere of 20 vol-% $CO_2$ in $N_2$ at a total flow rate of 50 mL $min^{-1}$. Due to the high volatility of the S source, the saturator containing pure $CS_2$ is cooled in an ice/NaCl bath (10:1 g $g^{-1}$, ca. −20 °C). In order to control the amount of $CS_2$ in the reactor feed, a gas flow between 2 mL $min^{-1}$ and 50 mL $min^{-1}$ is passed through the saturator once the reaction temperature was reached. It was ensured that a gas mixture of 20 vol-% $CO_2$ in $N_2$ at a total flow rate of 50 mL $min^{-1}$ was always obtained at the furnace entry. It should be noted that elemental S is produced by the doping procedure. Therefore a 100 mL 3-neck flask filled with glass-wool was placed at the reactor exhaust to catch volatile S and to avoid clogging of small-diameter exhaust lines. After the desired reaction time, the gas flow is switched to bypass the saturator, and the reactor is allowed to cool in a flow of 50 mL $min^{-1}$ $N_2$. Depending on the parental carbon and the reaction time, 280–310 mg of S doped carbon is obtained.

#### 2.4.3. P doping

For P doping, 350 mg of AC, CB or CNF are placed in the quartz reactor and heated to 825 °C at a rate of 10 C $min^{-1}$ and 50 mL $min^{-1}$ $H_2$ flow. After reaching the reaction temperature, the gas flow (50 mL $min^{-1}$ $H_2$) is switched to pass through the saturator containing trimethyl phosphite as P source before entering the furnace. Elemental P as well as $PO_x$ is produced by the doping procedure, thus a 100 mL 3-neck flask filled with glass-wool was placed at the reactor exhaust to catch volatile P species and avoid clogging of exhaust lines. After the desired reaction time (15–180 min), the gas flow is switched to bypass the saturator, and the reactor is allowed to cool under a flow of 50 mL $min^{-1}$ $N_2$. After the temperature falls below 80 °C, the gas is switched from $N_2$ to synthetic air for 12 h in order to ensure oxidation of any potentially formed white phosphorus. Depending on the parental carbon and the employed reaction time, between 280 and 320 mg of P doped carbon is obtained.

### 2.5. Pt loading

For loading of the doped CNFs with platinum nanoparticles, a modified method of Rampino and Nord was used [44]. To this end, 20 mg of carbon was mixed with 179 μL of a precursor solution containing chloroplatinic acid hexahydrate (32.9 mg) in ethanol (1 mL). Afterwards, 0.3 mL of ethanol was added to the mixture, before dispersing the carbon by 30 min of ultra-sonification. The solvent was evaporated in a vacuum oven at 60 °C and 50 mbar. In the following step, the supported chloroplatinic acid was reduced in a stream of 20 vol-% $H_2$ in $N_2$ (total flow 166 mL $min^{-1}$) for 2 h in a tubular furnace at 200 °C. The carbon-supported Pt catalysts were used for RDE testing without further purification or pre-treatment.

### 2.6. Rotating disc electrode testing

The stability of the synthetized materials at relevant electrochemical potentials was determined from electrochemical half-cell measurements. The setup consisted of a three-electrode compartment Teflon® cell with a rotating disk electrode (RDE) equipped with a Radiometer Analytical rotation controller (model Origatrod manufactured by Origalys) and a Gamry Reference 600 potentiostat. A graphite rod was used as counter electrode and a double junction Ag/AgCl (3 M KCl, Metrohm) electrode served as reference electrode. The cell compartment of the reference electrode was separated with a Nafion® membrane to avoid chloride ion leaching during the measurements. All potentials are reported with respect to the reversible hydrogen electrode (RHE). To ensure an accurate correction for the Ag/AgCl electrode potential, it was measured utilizing a Pt working electrode in an $H_2$-saturated electrolyte beforehand. This procedure was repeated for every measurement with the tested Pt/CNF catalysts.

The catalyst films were prepared by dispersing the catalyst powders in a mixture of 15% ultrapure isopropanol in ultrapure water using an ultrasonic vial treater (30 min initial, 10 min when re-used). Before sonication, a respective amount of a 5% Nafion® solution to reach an ionomer to carbon ratio (I/C ratio) of 0.1 was added to the dispersion. A 20 μL ink droplet was added onto the freshly polished glassy carbon disk electrode with a diameter of 5 mm (0.196 $cm^2$ geometrical surface area) of an RDE tip, and finally dried in air. The catalyst loading on the electrode was set to 10 $\mu g_{Pt}$ $cm^{-2}$. 0.1 M $HClO_4$ was used as the electrolyte. The ohmic drop was corrected via positive feedback.

The stability tests consisted of a voltage cycling-based accelerated stress test (AST) with 2000–5000 potential cycles at 1 V $s^{-1}$ between either 0.05 and 1.5 $V_{RHE}$ or 1.0 and 1.5 $V_{RHE}$. The degradation protocol was performed in $N_2$-saturated electrolyte [45] without rotation and the electrochemically active surface area (ECSA) was determined via CO-stripping initially and after 10, 100, 200, 500, 1000 and 2000 cycles, respectively. Before each stability measurement, the activity of the catalysts was determined. For activation, the films were subjected to 50 cleaning cycles (0.05–1.0 V) in $N_2$-saturated electrolyte. ORR activities were calculated from the anodic scan of a cyclic voltammogram recorded in $O_2$-saturated electrolyte with a scan rate of 50 mV $s^{-1}$ by Koutecký-Levich analysis at 0.9 $V_{RHE}$ while rotating the electrode at 1600 rpm. To separate the current related to oxygen reduction, the cyclic voltammograms were background corrected by subtracting a cyclic voltammogram recorded under nitrogen saturation within the same potential window. The ORR activity measurements were carried out according to the guidelines reported in literature [46]. The specific activity (SA) is reported as the kinetic current density normalized to the real Pt surface area, which is calculated from the electrochemical CO oxidation charge (CO stripping) assuming a surface charge density of 380 μC $cm_{Pt}^{-2}$. Mass activities (MA) were derived from the SA and ECSA.

### 2.7. Characterization

Nitrogen physisorption at −196 °C was conducted using a Micromeritics Tristar 3020 analyzer. Before physisorption analysis, samples were degassed overnight at 200 °C and 0.01 Torr. Specific surface areas were determined by the Brunauer-Emmett-Teller (BET) method. X-ray

powder diffraction was performed utilizing a Bruker D8 DaVinci diffractometer in Bragg-Brentano geometry with Cu Kα radiation. Raman spectroscopy was carried out utilizing a Horiba Jobin Yvon LabRAM HR800 Raman microscope, employing a HeNe laser with a wavelength of 633 nm. Fitting of the Raman spectra and extraction of $I_D/I_G$ ratios was performed according to Mallet-Ladeira et al. [47]. At least five spectra of different sites of each sample were recorded and evaluated. Elemental combustion analysis for determination of the N and S content of the doped carbons was carried out using a Vario El III (Elementar Analysesysteme) and an Elementar Unicube analyzer. Determination of P content was conducted by microwave digestion in aqua regia (Berghof SpeedWave XPERT) followed by microwave plasma atomic emission spectroscopy (Agilent 4210 MP-AES). Pt loadings of the supported Pt/CNFs were determined by inductive coupled plasma excited optical emission spectroscopy (ICP-OES) after aqua regia digestion (Optical Emission Spectrometer 2000 DV, PerkinElmer). Scanning transmission electron microscopy (STEM) micrographs were obtained on a Hitachi SU9000 electron microscope operating at an accelerating voltage of 30 kV. Energy-dispersive X-ray spectroscopy (EDS) maps were recorded at an accelerating voltage of 30 kV using an Oxford Ultim Extreme 100 $mm^2$ detector and a pixel dwell time of 400 µs. TEM images of supported Pt/CNF catalysts were recorded with a Philipps CM20 transmission electron microscope at an accelerating voltage of 200 kV. Particle sizes were determined using ImageJ by manually counting 300–500 particles. X-ray photoelectron spectroscopy (XPS) was conducted on a Kratos Analytical Axis Ultra DLD spectrometer using monochromatic Al Kα irradiation (1486.6 eV) operating the anode at 10 kV with an aperture of 700 x 300 µm. Surveys were recorded with a pass energy of 160 eV, while high-resolution spectra were measured with a pass energy of 20 eV. The energy axis was calibrated by fixing the C1s contribution of $sp^2$ carbon ("graphite") at 284.6 eV. For deconvolution, linear combinations of Gaussian and Lorentzian functions were utilized (pseudo-Voigt-profiles) and Shirley background subtraction was performed prior to fitting. For detailed fitting procedures, see the SI. Temperature programmed oxidation (TPO), desorption (TPD) and the determination of the amount of oxygen chemisorption sites were performed utilizing a NETZSCH STA 449 Jupiter thermogravimetric balance coupled to a NETZSCH Aëolos quadrupole mass spectrometer. TPO was conducted in a flow of 100 mL $min^{-1}$ synthetic air, employing a heating ramp of 5 °C $min^{-1}$. TPD was performed in a flow of 30 mL $min^{-1}$ Ar, utilizing a heating ramp of 5 °C $min^{-1}$. The amount of oxygen chemisorption sites was determined by heating the carbon sample to 300 °C with a heating ramp of 10 °C $min^{-1}$ in a mixed gas flow of 50 mL $min^{-1}$ air and 50 mL $min^{-1}$ Ar. After holding 300 °C for 1 h, the system was cooled to 50 °C with a cooling rate of 10 °C $min^{-1}$ and the system was flushed for 1 h with 300 mL $min^{-1}$ Ar. Subsequently, TPD was performed heating the sample at 10 °C $min^{-1}$ to 1200 °C in a stream of 30 mL $min^{-1}$ Ar. Quantification of evolved CO, $CO_2$ and $H_2O$ was realized by calibrating the coupled mass spectrometer by performing the TPD part of the program with calcium oxalate monohydrate as a standard.

## 3. Results and discussion

### 3.1. Starting materials

Activated carbon, carbon black and platelet-type carbon nanofibers were chosen as starting materials due to their high relevance for use as catalyst supports. The three starting materials exhibit different morphologies (Fig. 1a–c) as well as different textures, with AC being highly microporous (isotherm type Ib) exhibiting a specific surface area (SSA) of 1658 $m^2 g^{-1}$ (Fig. 1d). In contrast, $N_2$ physisorption isotherms of CB and CNF indicate the presence of micro-, meso- and macropores (isotherm type IVa), represented by interparticle spaces of different size, with SSA's of 189 and 123 $m^2 g^{-1}$, respectively. X-ray powder diffraction (XRD) of the pristine materials shows the typical reflections for $sp^2$ hybridized carbon for all three materials, among others the (002) contribution at 26°/2θ and the (100/101) reflections around 43°/2θ

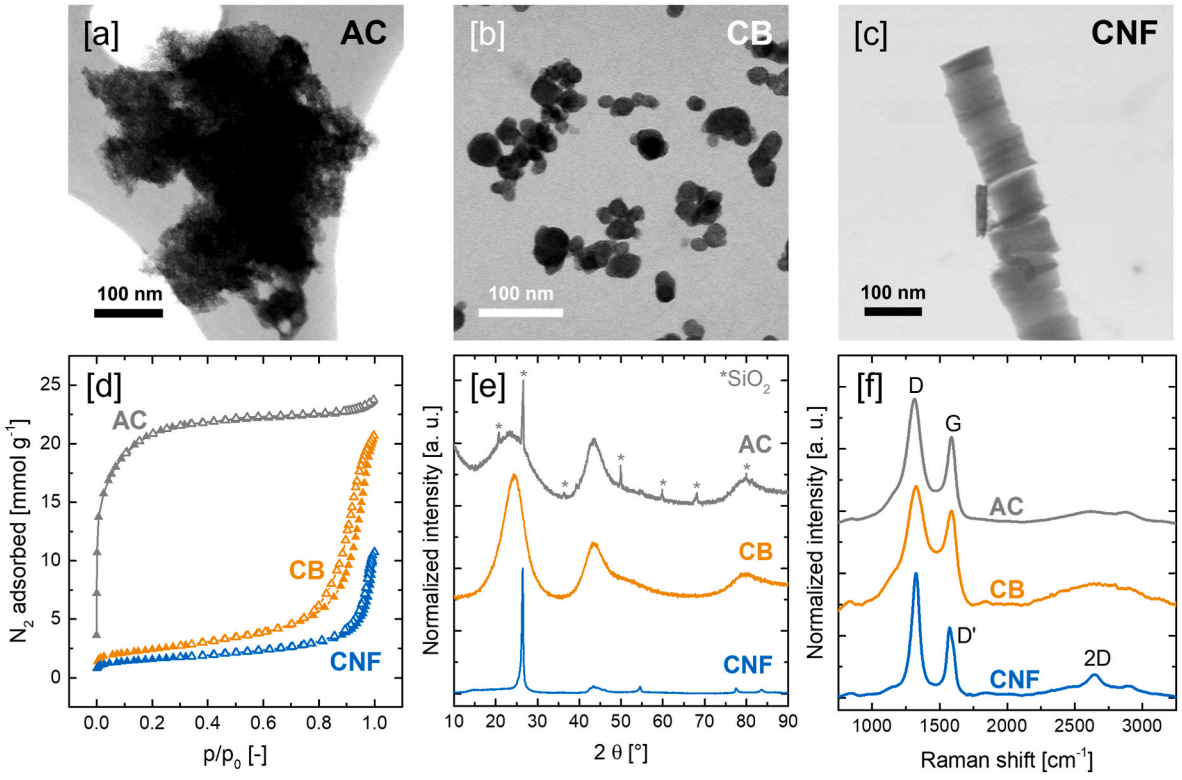


**Fig. 1.** STEM micrographs of the [a] activated carbon, [b] carbon black and [c] carbon nanofibers. [d] $N_2$ physisorption isotherms, [e] powder X-ray diffractograms and [f] representative Raman spectra of activated carbon, carbon black and CNF. (A colour version of this figure can be viewed online.)

(Fig. 1e). However, only CNF shows sharp reflections indicating a high degree of crystallinity, while CB and AC exhibit broad contributions with low signal-to-noise ratio that are characteristic for carbon materials lacking long-range structural order. It should be noted that the biomass-derived AC contains crystalline $SiO_2$ as impurity that was not removed by the applied demineralization procedure.

Similar to the XRD data, Raman spectroscopy implies low crystallinity for AC and CB, as indicated by broad D (~1320 $cm^{-1}$) and G (~1590 $cm^{-1}$) bands, high $I_D/I_G$ ratios (1.39 for AC, 1.31 for CB), and the absence of any developed second order contribution (Fig. 1f, S2a). In contrary, the Raman spectrum of CNF shows sharp D and G bands as well as a clear 2D (~2660 $cm^{-1}$) contribution thereby confirming its crystalline character. However, the high $I_D/I_G$ ratio (1.72 ± 0.06) and the pronounced D' (1620 $cm^{-1}$) band indicate comparatively low in-plane crystallite size as well as the presence of a high concentration of edge sites that is typical for platelet-type CNF [47]. Reflecting the general

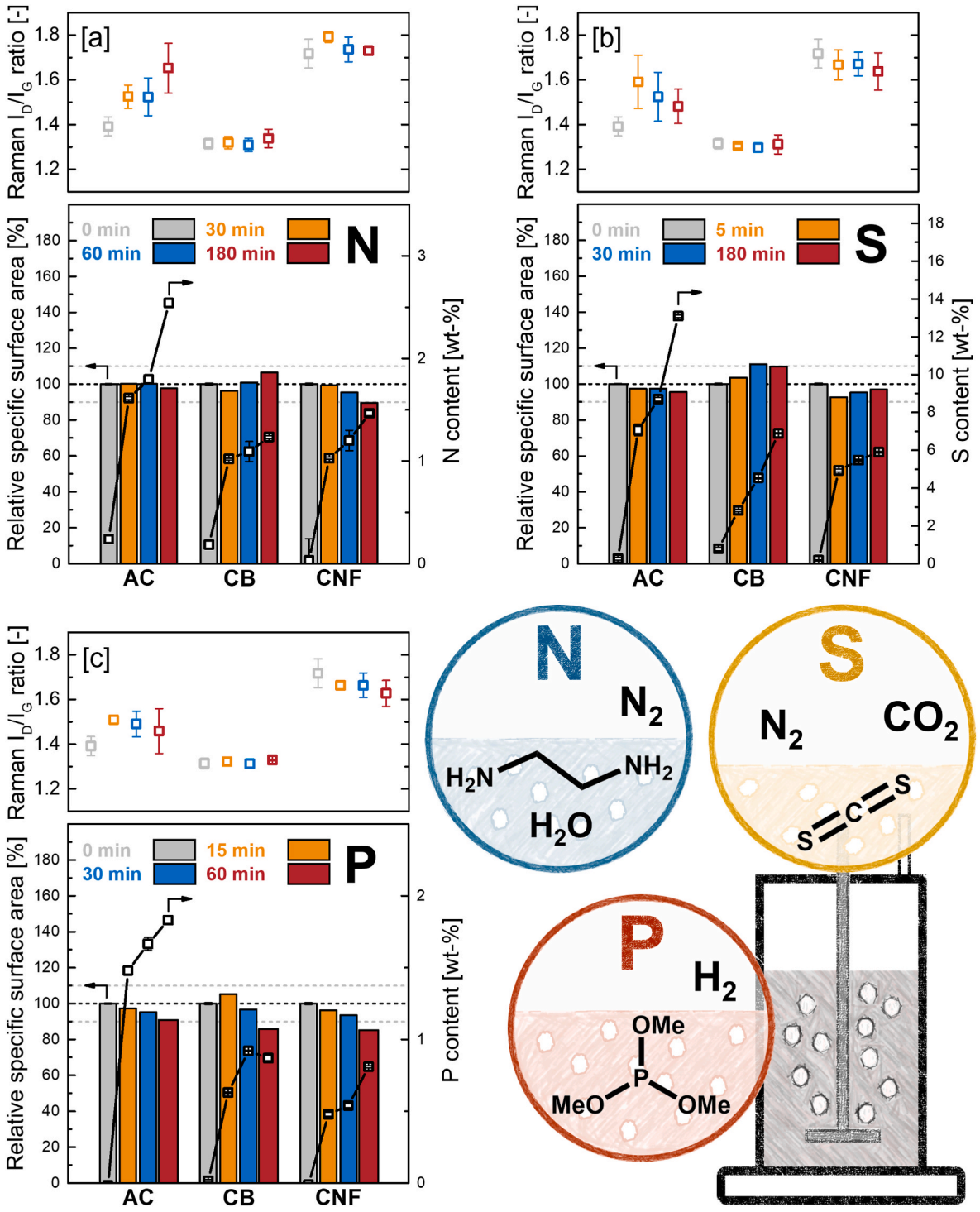


**Fig. 2.** Influence of gasification assisted heteroatom doping on texture, structure and heteroatom loading of AC, CB and CNF. The specific surface area relative to the pristine carbon materials serves as descriptor for textural changes, while the Raman $I_D/I_G$ ratio is used as descriptor for structural changes. The pristine carbons are subjected to GAHD for different periods of time. [a] N doping (875 °C, ethylene diamine/water vapor, $N_2$), [b] S doping (825–875 °C, $CS_2$ vapor, 20 vol-% $CO_2$ in $N_2$) and [c] P doping (825 °C, trimethyl phosphite vapor, $H_2$). (A colour version of this figure can be viewed online.)

trends in SSA and crystallinity, temperature programmed oxidation (TPO) in air shows that AC exhibits the lowest oxidation resistance with the maximum rate of mass loss at 592 °C, followed by CB at 613 °C and CNF at 636 °C (Fig. S2b). X-ray photoelectron spectroscopy was carried out to probe the surface composition of the materials, revealing that carbon and oxygen are the dominant surface species for pristine AC (95.6 at-% C, 3.8 at-% O), CB (94.0 at-% C, 6.0 at-% O) and CNF (93.6 at-% C, 5.7 at-% O) (Fig. S2c, Table S4). Other detectable elements were Si (0.2 at-%) in case of AC as well as Cl in case of AC (0.4 at-%) and CNF (0.7 at-%) stemming most likely from HCl treatments for demineralization or removal of the CVD catalyst, respectively. It should be noted that Cl could not be detected in any of the samples after the high-temperature heteroatom doping procedure. In addition, bulk elemental (combustion) analysis was carried out, showing that the bulk composition of AC, CB and CNF compares reasonably well with the surface composition (Table S4).

### 3.2. Heteroatom doping

Ethylene diamine (EDA), carbon disulfide ($CS_2$) and trimethyl phosphite (TMP) were chosen as precursors for N, S and P doping on basis of volatility, handling, elemental composition and toxicity. Considering the choice of gasification agents, $CS_2$ was combined with $CO_2$, while ethylene diamine was used with $H_2O$ to avoid formation of carbamates in presence of $CO_2$. TMP was paired with hydrogen, with the goal of facilitating the reduction of P and avoiding the deposition of non-volatile oxidized P species such as (poly)phosphates on the carbon surface. A parameter optimization was executed for each combination of dopant, gasification agent and carbon material, varying the dopant/gasification agent ratio and the reaction temperature with the aim to achieve heteroatom doping while retaining the properties of the parental carbon. In this context, the SSA as well as the Raman $I_D/I_G$ ratio and position of the G-band are utilized as descriptors for textural and structural integrity, respectively (see Fig. S3 for the exemplary optimization of doping conditions for the combination CNF/TMP/$H_2$). In all cases, the optimum temperature was located between 825 and 875 °C, well-above the onset for carbon (hydro-)gasification by $CO_2$, $H_2O$ and $H_2$ with sample burn-off usually around 10 wt-%, depending on carbon material and treatment duration [48,49]. It should be noted that heteroatom loading was determined by two different methods for each sample, utilizing elemental (combustion) analysis and MP-AES for determination of the bulk content and XPS for the surface content.

Under optimized conditions (875 °C, mixture of EDA:$H_2O$ 1:1.5 mol $mol^{-1}$ in the saturator, $N_2$ atmosphere), N doping could be achieved for AC, CB and CNF. By increasing treatment times from 30 to 180 min, up to 2.5 wt-% of N could be incorporated into AC as indicated by elemental (combustion) analysis, accompanied by a decline in SSA of only 2.3%, which is close to the measurement error of approximately 0.5% (Fig. 2a, see Table S5 for XPS quantification results). Compared to AC, lower N doping amounts were achieved for CB (1.2 wt-% at 180 min) and CNF (1.5 wt-% at 180 min). However, changes in SSA remained minor also for CB and CNF (+6.4% for CB; −10.4% for CNF). The texture was found to be changed insignificantly by the N doping procedure as indicated by total pore volume and the shape of the $N_2$ physisorption isotherms (Fig. S4). It should be noted, that the texture of the examined carbons is subject to processes that work in opposite directions. Deposition of non-volatiles originating from the heteroatom sources is causing a decrease in SSA and pore volume by blocking micropores and interparticle spaces. This is observed in all cases if no gasification agent is present. A process that works towards increasing the SSA is carbon gasification, as at high temperatures and concentrations, the gasification agent will not only remove non-volatile deposits, but will also attack the carbon backbone. A third process influencing the texture during GAHD is the exchange of carbon surface atoms with heteroatoms. Depending on the similarity of atomic radii and bond lengths to the radius of the carbon atom and the C═C bond length, this exchange will cause distortions in the hypothetical, perfectly planar graphene plane, whereas dopants of higher atomic radius such as S and P are expected to cause more pronounced changes in SSA compared to N. However, we expect all three mentioned processes to play a role during GAHD, but as the experimental conditions were optimized to cause minimal changes in SSA, those processes responsible for increasing the SSA are mostly in equilibrium with those causing a decrease in SSA.

The Raman $I_D/I_G$ ratio was found to increase significantly for AC from 1.39 to 1.65 with increasing treatment duration, indicating a decline in structural order (Fig. 2a). CB and CNF in contrary show only insignificant changes in $I_D/I_G$ ratios after 180 min of gasification-assisted N doping. The observation of only minor changes in structural descriptors such as $I_D/I_G$ ratio or the position of the G-band (Fig. S5) after heteroatom doping might be ascribed to the fact that only the surface of the carbon materials is affected by the treatment. As the surface of the studied carbons is inherently rich in defects such as edge sites and curved/distorted graphene layers/stacks the exchange of one defect site (carbon edge site) against another (heteroatom) might not change structural descriptors such as the $I_D/I_G$ ratio and the position of the G-band, especially when the bulk of the sample remains unaffected by the treatment. We hypothesize that the unaffected bulk is the main reason why changes in $I_D/I_G$ ratio as well as in the position of the G-band are insignificant for CB and CNF, as the atomic ratio of $C_{surface}/C_{bulk}$ is expected to be low, meaning that changes that only affect the surface are not picked up by Raman spectroscopy. The $C_{surface}/C_{bulk}$ ratio is expected to be much higher for AC, which in turn leads to an increased response of structural descriptors such as $I_D/I_G$ ratio or position of the G-band upon heteroatom doping.

It should be noted that the general trends in the achievable heteroatom loading AC > CB ≈ CNF as well as the structural stability under doping/gasification conditions CNF ≈ CB > AC appear to be influenced solely by the properties of the individual carbon materials, thus remaining valid for other combinations of dopant and gasification agent. In this context, by varying treatment duration of gasification-assisted S doping (825 °C for AC and CNF, 875 °C for CB; $CS_2$ in the saturator, 20 vol-% $CO_2$ in $N_2$ atmosphere) remarkably high S loadings of up to 13.1 wt-% could be achieved for AC, accompanied by a decrease in SSA of only 4.4% (Fig. 2b, see Table S6 for XPS quantification results). Likewise, high S loadings of up to 6.9 wt-% and 5.9 wt-% could be obtained for CB and CNF, respectively, while inducing only minor changes in SSA (+9.8% for CB, −2.9% for CNF). Total pore volume and the shape of the $N_2$ physisorption isotherms were found to be unaffected by the S doping procedure in most cases (Fig. S4). As already described for N doping, AC showed larger changes in the $I_D/I_G$ ratio (from 1.39 for pristine AC, to over 1.59 at 5 min, to 1.48 at 180 min treatment duration) with increasing treatment duration compared to CB and CNF, which remained largely unaffected by the combined influence of S doping and gasification (Fig. 2b).

In comparison to N and S doping, the retention of the texture during P doping proved to be more challenging. By varying the treatment duration under optimized doping conditions (825 °C, TMP in the saturator, $H_2$ atmosphere), a P loading of up to 1.9 wt-% could be achieved for AC while the SSA decreased simultaneously by 9.1% (Fig. 2c, see Table S7 for XPS quantification results). For CB and CNF, P loadings of up to 0.9 and 0.8 wt-% could be obtained, respectively, with SSA dropping by 14.2% in case of CB and 14.7% for CNF. For AC and CNF, textural changes were limited to a decreased micropore volume as indicated by a lower $N_2$ uptake in the relative pressure range $0<p/p_0<0.1$ of physisorption isotherms with increased treatment duration (Fig. S4). In addition to a decreasing micropore volume, CB additionally showed a decrease in the meso-/macropore volume with increasing P loading, with the $N_2$ uptake in physisorption isotherms decreasing in the range of $0.8<p/p_0<1.0$. The formation of a plateau in the desorption branch between $0.85<p/p_0<1.0$ for CB treated for 60 min indicates narrowing pore necks (e. g. formation of ink bottle pores). The decreasing micropore volumes for AC, CB and CNF as well as the

narrowing of pore necks for CB indicate at least a partial deposition of P species on top of the carbon surface. Despite changes in texture, the structural integrity of the carbons remained largely intact, as with increasing P doping treatment duration only minor changes in $I_D/I_G$ ratio could be detected for AC, while structural changes for CB and CNF remained insignificant(Fig. 2c).

Independent of carbon material and dopant, the heteroatom loading could be adjusted within a specific range by varying the treatment duration and thus the overall amount of dopant exposure of the carbons. Especially the sulfur doping procedure allowed wide-range tuning of the heteroatom content depending on the amount of $CS_2$ supplied (Fig. S6). Considering the accessible heteroatom loading ranges of different carbon materials treated with an individual dopant on one hand and of one carbon material treated with different dopants on the other hand, it may be concluded that the loading range is dependent on both, the nature of the dopant/gasification agent system as well as on the characteristics of the treated carbon material.

It should be noted that dual doped carbons are accessible by simply running individual GAHD procedures in sequence. Utilizing CNF as model material, all possible combinations of dual doping for N, S and P could be achieved even with non-optimized (for dual doping) reaction conditions. Reaction conditions, Raman spectroscopy, $N_2$ physisorption and XPS analysis of dual doped carbons are summarized in Tables S2 and S8 and Figs. S7–10.

### 3.2.1. Analysis of introduced heteroatom species

In order to examine the heteroatom species and their distribution introduced by GAHD, EDS mapping, XPS and high-temperature TPD-MS were employed. As shown exemplarily by EDS mapping of CNF doped with N, S and P, gasification-assisted heteroatom doping affords a homogeneous surface distribution of heteroatom species (Fig. 3a–c). XPS analysis of the N doped carbons reveals the presence of pyridinic, pyrrolic, quaternary as well as oxidized N species for all carbon materials (Fig. 3d, S11). Independent of the utilized carbon and the treatment duration, the distribution of the individual N species was found to be similar, with pyridinic N being the dominant species (~50%) followed by pyrrolic (~20%) and quaternary (~20%) N, with oxidized N species (10%) playing a minor role (Fig. S12). High-temperature TPD-MS to up to 1400 °C revealed that most of the introduced N species are quite temperature stable, with similar desorption ranges of 800–1400 °C and a desorption maximum around 1100 °C for all carbons(Fig. S13). In addition, the desorption profile of AC shows some low-temperature NO evolution in the temperature range between 300 and 600 °C, indicating decomposition of oxidized N species [50]. Given the decomposition temperature ranges of pyridinic (900–1000 °C) [39,51], pyrrolic (700–900 °C) [39,50] and quaternary N (1000–1500 °C) [52,53] reported in literature, the results of high-temperature TPD are in agreement with those of XPS analysis.

Gasification-assisted S doping yields aliphatic sulfides, thiophenic S as well as oxidized S species such as sulfones and sulfoxides. XPS analysis reveals that thiophenic S is dominating (≥85%) the ensemble regardless of the treatment duration and carbon material (Fig. 3e, S14-15). This finding is reflected by high-temperature TPD-MS up to 1400 °C, showing decomposition of a large fraction of S species in the temperature range of 600–1400 °C, indicating the presence of comparatively temperature stable aromatic S species (Fig. S16) [54,55]. While the surface of CNF appears to be largely occupied by thiophenic S, CB and AC additionally show significant low-temperature desorption of S species, hinting at the presence of thioles (227–377 °C) [56], aliphatic sulfides (350–620 °C) [57], as well as oxidized S as present in sulfones and sulfoxides (~400 °C) [58]. Given the highly microporous character of AC, even a low amount of weakly adsorbed and unreacted $CS_2$ could be detected. XPS analysis revealed the presence of at least two types of P species, which differ in their state of oxidation (Fig. 3f, S17-18). The reduced P species, corresponding to a stoichiometry of $C_3PO_1$ (triphenylphosphine oxide may serve as a model compound with similar binding energy) [59] proved to be the dominant species for all P doped samples, representing ~75% of the P species ensemble. The second species corresponds to P in a higher state of oxidation, showing binding energies that compare well to stoichiometries such as $C_{0-1}PO_{3-4}$, with P bound to C either via only one direct bond, or via ether-type bridge--oxygen [59–61].

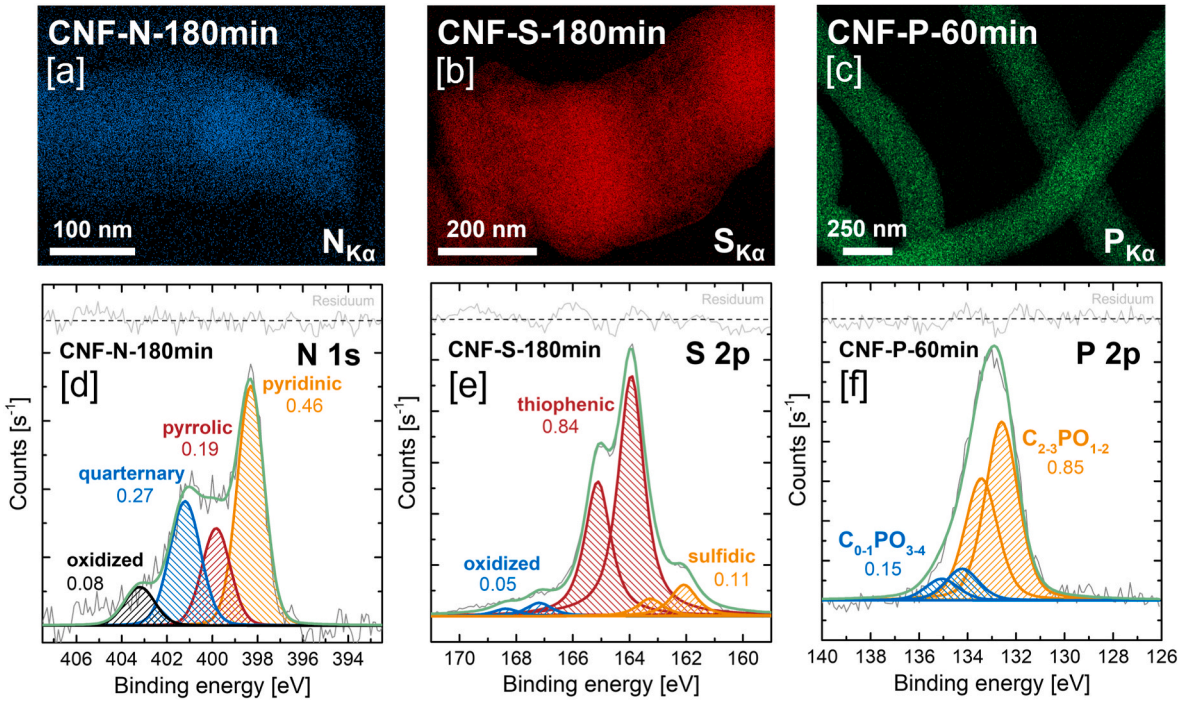


**Fig. 3.** EDS elemental maps of CNF subjected to gasification-assisted [a] N, [b] S and [c] P doping. Exemplary high-resolution XPS [d] N 1s, [e] S 2p and [f] P 2p spectra of heteroatom doped CNF. (A colour version of this figure can be viewed online.)

### 3.2.2. The role of carbon defect sites for gasification-assisted heteroatom doping

Gasification-assisted heteroatom doping relies on the hypothesis that the simultaneous presence of a heteroatom source and a gasification agent allows the atomic replacement of carbon atoms against heteroatoms, assuming that the gasification agent introduces defects/chemisorption sites that are subsequently saturated by the dopant. To probe this hypothesis, the amount of chemisorption sites was determined for the pristine carbon materials, and was subsequently compared to the amount of N, S and P incorporated into the different carbon materials. This comparison allows to estimate if the gasification agents introduced new defect sites into the carbon materials that could serve as chemisorption sites for the dopants.

The amount of available chemisorption sites in the pristine materials was determined by loading the carbons with oxygen at 300 °C followed by TPD-MS to quantify desorbed oxygen in form of $CO_2$, CO and $H_2O$ (cf. SI for detailed information) [62,63]. As expected, AC showed by far the highest amount of oxygen chemisorption sites (2670 μmol $g^{-1}$), with CNF (1738 μmol $g^{-1}$) and CB (1387 μmol $g^{-1}$) exhibiting a significantly lower mass-based site density (Fig. 4a). Considering the surface occupation of a chemisorption site (assumed to be identical to the area occupation of an edge carbon atom lying in the (100) plane (0.083 $nm^2$)) [64], the fraction of the total surface area susceptible to oxygen chemisorption termed "active surface area" (ASA) can be determined. In this context, CNF shows the largest ASA (71% of SSA) due to the high edge site exposure of platelet-type CNF, followed by CB (37% of SSA) and AC (8% of SSA) (Fig. 4a). Utilizing the heteroatom loading and the amount of chemisorption sites determined for pristine AC, CB and CNF, the degree of defect/chemisorption site saturation was calculated for every heteroatom doped carbon (Fig. 4b). In this context, very similar degrees of chemisorption site saturation are reached for N (0.4–0.7 mol $mol^{-1}$) and P doping (0.1–0.25 mol $mol^{-1}$) regardless of the employed carbon material. This indicates that the accessible degree of chemisorption site saturation is determined by the employed combination of dopant/gasification agent. In case of N and P doping, the amount of achievable heteroatom loading is thus governed by the initial amount of chemisorption sites available in each carbon. The degree of chemisorption site saturation below 1 mol $mol^{-1}$ implies that no new chemisorption sites are generated in case of the employed N and P doping procedures which, however, does not mean that the presence of the gasification agent is dispensable: For both N and P doping, it was found that the absence of $H_2O$ and $H_2$ reduces the SSA and the pore volume significantly for all carbons. Consequently, the gasification agents impede the degradation of carbon texture by removing undesired deposits from the carbon surface. Contrary to N and P doping, S doping with $CS_2/CO_2$ affords much higher degrees of chemisorption site saturation for all carbon materials, with values exceeding 1 mol $mol^{-1}$ indicating the introduction and subsequent S saturation of new chemisorption sites. For CNF, a degree of chemisorption site saturation of 1 is not exceeded substantially, however, in light of the extremely high fraction of SSA susceptible to chemisorption, the generation of additional defects by gasification might be impeded simply by a lack of unoccupied surface area.

### 3.3. Accelerated stress testing of N, S, P-doped CNF-supported Pt catalysts in the oxygen reduction reaction

To demonstrate the versatility of GAHD to study the isolated influence of heteroatom doping on the performance of carbon supported catalysts, the N, S and P content of CNF was precisely adjusted to 1.5 at-%, resulting in a series of catalyst supports featuring similar textures and structures but different surface chemistry. CNF were chosen as model support in order to limit diffusion limitations that are associated with the high microporosity of AC, and to allow a higher heteroatom loading than CB did permit (as determined by XPS, compare Tables S5–S7). As a reference, pristine CNF treated with $H_2$ at high temperatures (CNF–H) was utilized, representing a carbon surface mostly terminated by hydrogen (Fig. 5, S19-21 and Table S9).

The electrochemical oxygen reduction was chosen as a test reaction and platinum nanoparticles in the size range of 1.4–1.8 nm were deposited onto the heteroatom doped CNF (Fig. 6a, S22 and Table S10). XPS analysis of the Pt/C catalysts showed a similar C/heteroatom atomic ratio for CNF–N-1.5 before and after Pt loading, while a significant increase was detected for CNF–S-1.5 and CNF–P-1.5 after Pt loading, indicating preferential attachment of Pt nanoparticles on S and P surface species (Fig. S21, Table S9). Analysis of the XPS S 2p contribution of Pt/CNF–S-1.5 shows a decline in the relative amount of thiophenic S, pointing at thiophenic S species as Pt anchoring sites. In case of Pt/CNF–P-1.5, no shift in the relative amount of P species was observed by analysis of the XPS P 2p contribution, suggesting that Pt attachment

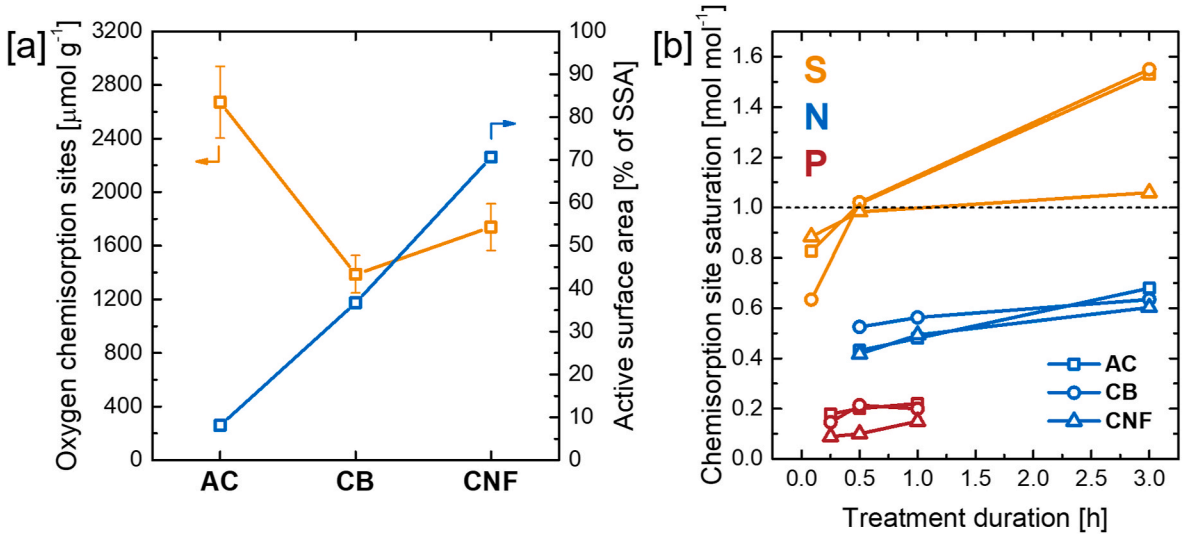


**Fig. 4.** [a] Amount of oxygen chemisorption sites in pristine AC, CB and CNF as determined by oxygen loading of the materials at 300 °C and subsequent quantification of the formed surface oxides by TPD-MS. The active surface area represents the fraction of the total surface area susceptible to oxygen chemisorption, taking into account the area occupation of an individual oxygen atom. [b] Fraction of chemisorption sites saturated by heteroatoms after the doping with N, S or P, comparing the amount of oxygen chemisorption sites of pristine AC, CB and CNF and the loading of N, S and P after gasification-assisted heteroatom doping. (A colour version of this figure can be viewed online.)

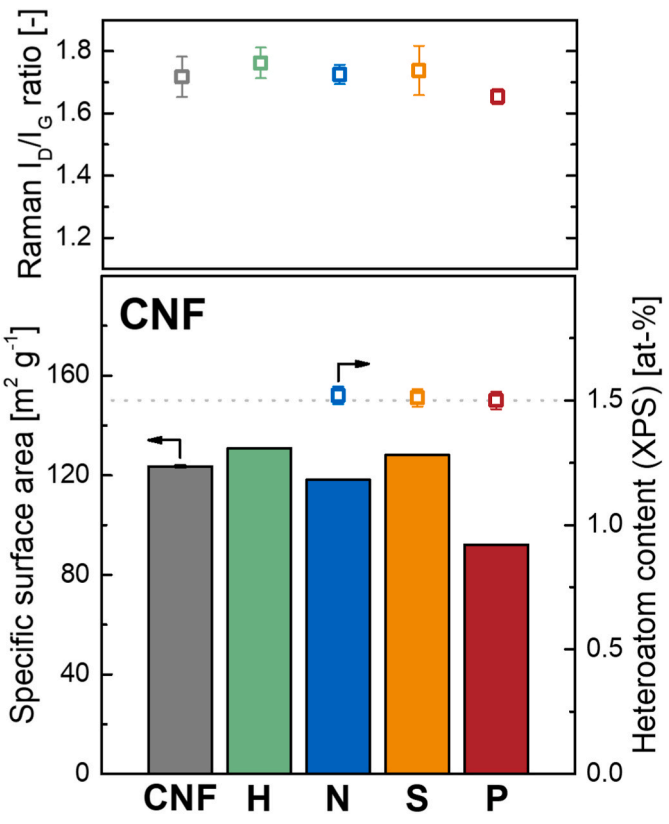


**Fig. 5.** Specific surface area, heteroatom loading, and Raman $I_D/I_G$ ratio of heteroatom doped CNF utilized as comparable catalyst support for Pt nanoparticles. (A colour version of this figure can be viewed online.)

occurs in equal proportions on oxidized and reduced P species (Fig. S21). Deconvolution of the XPS Pt 4f contributions of the different pre-reduced Pt/C catalysts yielded differences in the ratio of $Pt^0/Pt^{2+/4+}$, however, this ratio is influenced by re-oxidation after the reduction step and is in addition not representative for the oxidation state of Pt during potential cycling (Figs. S23–24). The binding energies of $Pt^0$, $Pt^{2+}$ and $Pt^{4+}$ were found to be similar for all supports, indicating that charge transfer does not play a significant role.

The specific ORR activities (normalized to the Pt surface) of the Pt/C catalysts determined at 0.9 $V_{RHE}$ were found to be in a range between 0.28 and 0.44 mA $cm^{-2}$, which compares well to similar Pt/C catalysts reported in literature (Table S10, for electrochemical characterization see Figs. S25–26) [3]. The influence of heteroatom doping on the stability of these model catalysts was probed by accelerated stress tests in the potential ranges from 1.0 to 1.5 $V_{RHE}$ (AST-1.0) as well as from 0.05 to 1.5 $V_{RHE}$ (AST-0.05), whereas the relative loss of ECSA served as a descriptor of catalyst degradation (Fig. 7). Two different potential ranges were chosen to selectively probe catalyst degradation by carbon corrosion related pathways in the potential range of AST-1.0, while AST-0.05 was conducted to examine the superposition of catalyst degradation related to Pt dissolution and particle growth pathways as well as carbon corrosion [65].

Hence, loss of ECSA during AST-1.0 can be attributed to degradation mechanisms related to carbon corrosion and secondary effects such as aggregation and detachment of Pt nanoparticles [42,66]. The N, S and P doped Pt/CNF catalysts show a similar degradation rate compared to the non-doped Pt/CNF–H (Fig. 7a, S27). TEM analysis of the Pt/C catalysts shows a similar increase in the average Pt particle diameter from 1.4 to 1.8 nm for the pristine materials to ca. 3 nm for all catalysts after AST-1.0 (Fig. S28). Besides Pt particle growth, detachment of Pt particles from the CNF supports as well as Pt aggregation was observed in all samples (Fig. 6b, S29). These results indicate that heteroatom doping of carbon supports with N, S or P might not be a viable approach for enhancing the resistance of Pt/CNF catalysts toward carbon corrosion induced degradation. This finding is in line with results of Hornberger et al., who could not observe any increase in stability of Pt supported on N doped carbon black toward carbon corrosion upon potential cycling from 1.0 to 1.5 $V_{RHE}$ [3].

Potential cycling from 0.05 to 1.5 $V_{RHE}$ probes the superposition of all possible catalyst degradation mechanisms such as the carbon support oxidation and related Pt nanoparticle detachment and agglomeration as well as Pt dissolution and Ostwald ripening [42,66]. Compared to AST-1.0, AST-0.05 yields clear differences in Pt/CNF catalyst stability depending on the surface chemistry of the CNF support (Fig. 7b, S30). In this context, Pt/CNF–S-1.5 and Pt/CNF–P-1.5 show a significantly reduced deactivation tendency compared to the reference Pt/CNF–H, indicated by a retention of 46% and 44%, respectively, of the initial ECSA after 2000 potential cycles while only 34% were retained in case of Pt/CNF–H. Overall degradation was most severe in case of Pt/CNF–N-1.5, whereas only 29% of the initial ECSA was available after AST-0.05. It should be noted that these findings compare well with the XPS analysis of the Pt/C catalysts, which suggested a higher degree of interaction between Pt and S and P doped CNF compared to the N doped support. TEM analysis of the Pt/C catalysts after AST-0.05 revealed Pt particle detachment as well as particle growth and agglomeration for all samples (Fig. 6c, S29). Comparing the average Pt particle sizes after AST-0.05, only minor differences between the heteroatom doped supports are observed. However, the particle size distributions differ significantly between the supports with Pt/CNF–H and Pt/CNF–P-1.5 showing unimodal distributions with a high amount of Pt particles exhibiting diameters between 2 and 4 nm (Fig. 8). Pt/CNF–N-1.5 shows a bimodal size distribution centered at Pt particle diameters of 2 nm and

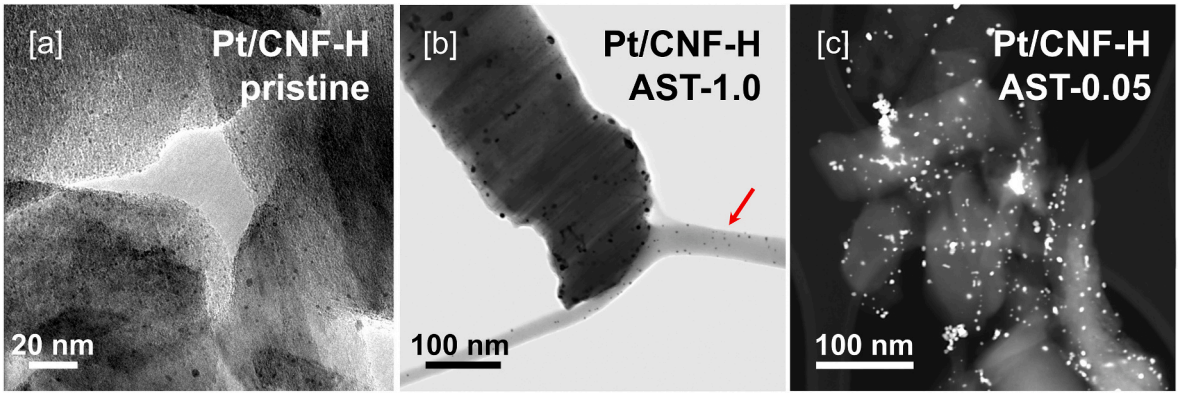


**Fig. 6.** TEM brightfield images of [a] pristine CNF–H loaded with Pt nanoparticles and [b] Pt/CNF–H after AST-1.0. The red arrow marks detached Pt nanoparticles in a film of ionomer. [c] TEM high-angle annular darkfield image of Pt/CNF–H after AST-0.05. (A colour version of this figure can be viewed online.)

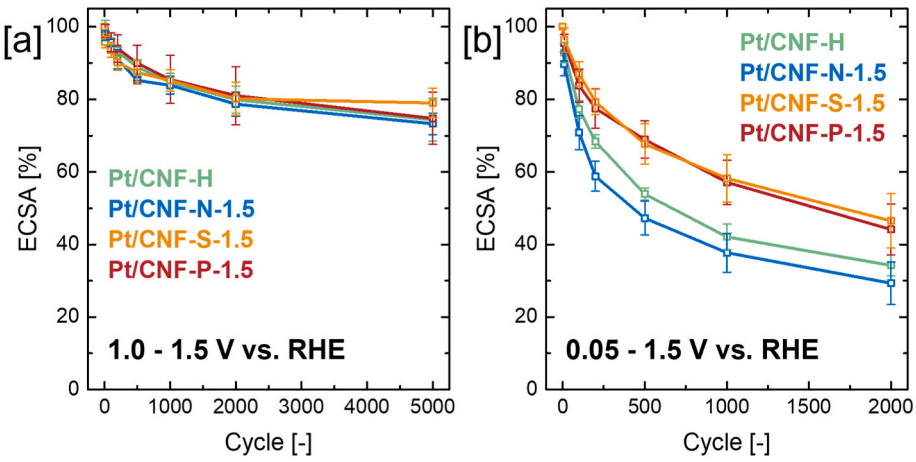


**Fig. 7.** [a] Accelerated stress test of 5000 potential cycles between 1.0 and 1.5 $V_{RHE}$ and [b] of 2000 potential cycles between 0.05 and 1.5 $V_{RHE}$ of Pt nanoparticles supported on different heteroatom doped CNF. Accelerated stress tests were conducted utilizing a RDE three-electrode setup in $N_2$ saturated 0.1 M $HClO_4$. ECSAs were determined by CO stripping. (A colour version of this figure can be viewed online.)

5 nm, while Pt/CNF–S-1.5 exhibits a very high proportion of Pt particles <3 nm, but at the same time a low number of very large (>10 nm) particles. Overall, these results compare well with literature reports, which implied an increased stability of Pt supported on S doped carbon supports [27,67] and no benefit of N doping [3,68].

AST-0.05 clearly shows the potential of using comparable model supports prepared by GAHD to isolate the effects of heteroatom doping on catalyst performance. The results indicate that the rate of loss of ECSA of Pt/CNF catalysts depends strongly on the nature of the heteroatom dopant, with N doping apparently accelerating catalyst degradation, and P and S doping impeding it. Notably, it is Pt/CNF–S-1.5 and Pt/CNF–P-1.5 which show the best overall performance in AST-0.05, even though S and P species are normally considered potent catalyst poisons for Pt. However, in this case both appear to be firmly

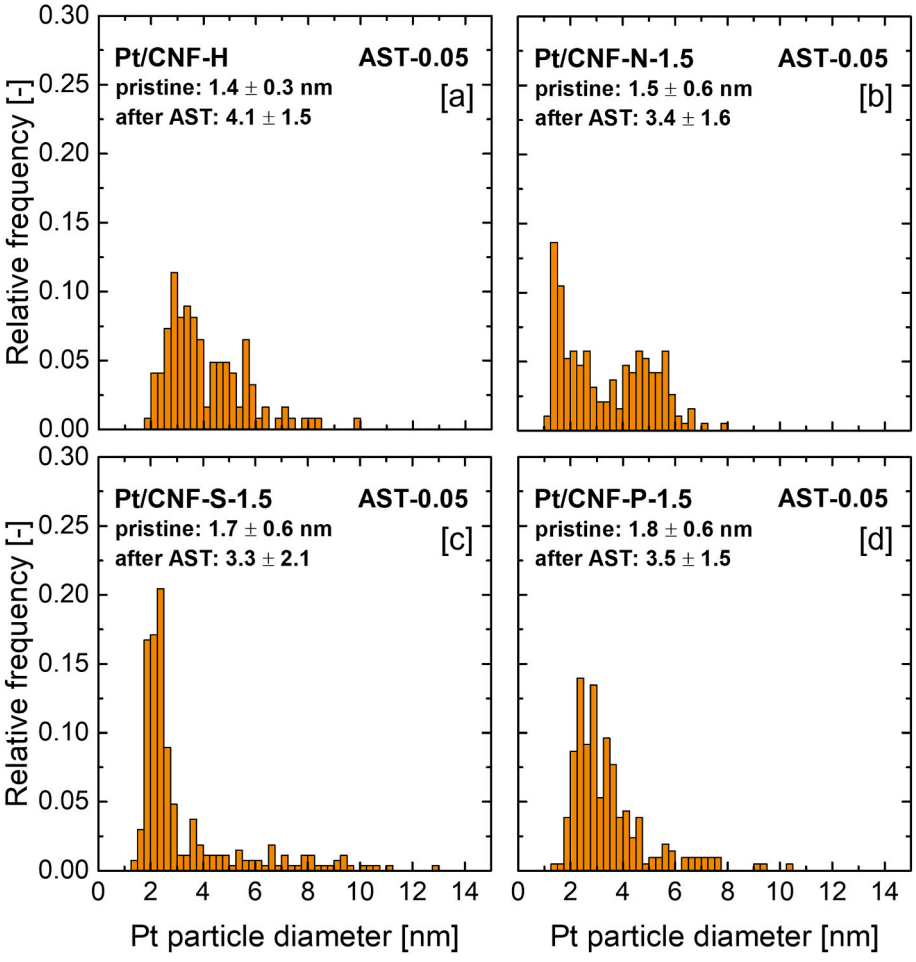


**Fig. 8.** Pt particle size distributions of [a] Pt/CNF–H, [b] Pt/CNF–N-1.5, [c] Pt/CNF–S-1.5 and [d] Pt/CNF–P-1.5 after AST-0.05. (A colour version of this figure can be viewed online.)

incorporated into the carbon matrix, whereas the decreased deactivation tendency indicates that the strong interaction of S and P with Pt can indeed be used to advantage.

## 4. Conclusion

A broadly applicable post-synthesis carbon heteroatom doping approach was developed, enabling incorporation of N, S and P into carbon materials of widely differing properties, while inducing only minimal changes in texture and nanostructure. The simultaneous reaction of a heteroatom source and a gasification agent with carbon surfaces enables an atomic replacement of carbon surface atoms with heteroatoms, allowing, for example, incorporation of up to 13.1 wt-% S into an activated carbon at a change of specific surface area of only 4.4%. The feasibility of GAHD to produce heteroatom doped model carbons to study the isolated effects of heteroatom dopants on the performance of carbon supported catalysts could be demonstrated by employing the electrochemical oxygen reduction reaction as a test reaction. It could be shown that the stability of electrocatalysts prepared by deposition of Pt nanoparticles on comparable N, S and P doped CNF depends strongly on the nature of the dopant. In this context, S and P doping of carbon catalyst supports was found to represent a viable approach toward Pt-based fuel cell catalysts of enhanced degradation resistance, while N doping increased the rate of ECSA loss. In this work, we demonstrated the high potential of GAHD to gain valuable insights into the impact of carbon heteroatom doping in a wide variety of applications, ranging from energy storage to electrocatalysis and thermal catalysis.

## Associated content

Supporting Information: Detailed XPS fitting procedure; detailed synthesis conditions for every heteroatom doped carbon; experimental setup for gasification assisted heteroatom doping; additional characterization ($N_2$ physisorption, XPS, TPO, high temperature TPD-MS, TEM, ICP-OES) of the pristine carbon materials, the heteroatom doped carbon materials, the dual doped carbon materials as well as the Pt/CNF catalysts; electrochemical characterization of Pt/CNF catalysts.

## CRediT authorship contribution statement

**Felix Herold:** Conceptualization, Investigation, Formal analysis, Writing – original draft, Funding acquisition. **Timo Imhof:** Investigation, Formal analysis, Writing – original draft. **Paul Roumeliotis:** Investigation, Formal analysis, Writing – review & editing. **Patrick Schühle:** Investigation, Formal analysis, Writing – review & editing. **Marc Ledendecker:** Supervision, Project administration, Funding acquisition, Writing – review & editing. **Magnus Rønning:** Conceptualization, Supervision, Project administration, Funding acquisition, Writing – review & editing.

## Declaration of competing interest

The authors declare that they have no known competing financial interests or personal relationships that could have appeared to influence the work reported in this paper.

## Acknowledgements

FH acknowledges a fellowship within the Walter-Benjamin-program of the Deutsche Forschungsgemeinschaft (DFG, German Research Foundation, project number 471263729). TI and ML acknowledge the German federal ministry for economy and energy (Bundesministerium für Wirtschaft und Energie (BMWi)) for funding within the scope of project FKZ 03ETB027G, POREForm. The Research Council of Norway is acknowledged for the support to the Norwegian Micro- and Nano-Fabrication Facility, NorFab, project number 295864.

## Appendix A. Supplementary data

Supplementary data to this article can be found online at https://doi.org/10.1016/j.carbon.2023.03.023.

## References

[1] Y. Yuan, Z. Chen, H. Yu, X. Zhang, T. Liu, M. Xia, R. Zheng, M. Shui, J. Shu, Heteroatom-doped carbon-based materials for lithium and sodium ion batteries, Energy Storage Mater. 32 (2020) 65–90, https://doi.org/10.1016/j.ensm.2020.07.027.

[2] S. Ghosh, S. Barg, S.M. Jeong, K. Ostrikov, Heteroatom-doped and oxygen-functionalized nanocarbons for high-performance supercapacitors, Adv. Energy Mater. 10 (2020), 2001239, https://doi.org/10.1002/aenm.202001239.

[3] E. Hornberger, T. Merzdorf, H. Schmies, J. Hübner, M. Klingenhof, U. Gernert, M. Kroschel, B. Anke, M. Lerch, J. Schmidt, A. Thomas, R. Chattot, I. Martens, J. Drnec, P. Strasser, Impact of carbon N-doping and pyridinic-N content on the fuel cell performance and durability of carbon-supported Pt nanoparticle catalysts, ACS Appl. Mater. Interfaces 14 (2022) 18420–18430, https://doi.org/10.1021/acsami.2c00762.

[4] K. Ham, S. Chung, J. Lee, Narrow size distribution of Pt nanoparticles covered by an S-doped carbon layer for an improved oxygen reduction reaction in fuel cells, J. Power Sources 450 (2020), 227650, https://doi.org/10.1016/j.jpowsour.2019.227650.

[5] U.I. Kramm, I. Herrmann-Geppert, J. Behrends, K. Lips, S. Fiechter, P. Bogdanoff, On an easy way to prepare metal-nitrogen doped carbon with exclusive presence of MeN4-type sites active for the ORR, J. Am. Chem. Soc. 138 (2016) 635–640, https://doi.org/10.1021/jacs.5b11015.

[6] G. Wu, K.L. More, C.M. Johnston, P. Zelenay, High-performance electrocatalysts for oxygen reduction derived from polyaniline, iron, and cobalt, Science 332 (2011) 443–447, https://doi.org/10.1126/science.1200832.

[7] J. Liu, W. Li, R. Cheng, Q. Wu, J. Zhao, D. He, S. Mu, Stabilizing Pt nanocrystals encapsulated in N-doped carbon as double-active sites for catalyzing oxygen reduction reaction, Langmuir 35 (2019) 2580–2586, https://doi.org/10.1021/acs.langmuir.8b03947.

[8] H. Cui, Y. Guo, L. Guo, L. Wang, Z. Zhou, Z. Peng, Heteroatom-doped carbon materials and their composites as electrocatalysts for CO 2 reduction, J. Mater. Chem.A 6 (2018) 18782–18793, https://doi.org/10.1039/C8TA07430E.

[9] Q. Cheng, N. Zhao, S. Lyu, Y. Tian, F. Gao, L. Dong, Z. Jiang, J. Zhang, N. Tsubaki, X. Li, Tuning interaction between cobalt catalysts and nitrogen dopants in carbon nanospheres to promote Fischer-Tropsch synthesis, Appl. Catal., B 248 (2019) 73–83, https://doi.org/10.1016/j.apcatb.2019.02.024.

[10] H.J. Schulte, B. Graf, W. Xia, M. Muhler, Nitrogen- and oxygen-functionalized multiwalled carbon nanotubes used as support in iron-catalyzed, high-temperature fischer-tropsch synthesis, ChemCatChem 4 (2012) 350–355, https://doi.org/10.1002/cctc.201100275.

[11] S. Louisia, R.C. Contreras, M. Heitzmann, M. Rosa Axet, P.-A. Jacques, P. Serp, Sequential catalytic growth of sulfur-doped carbon nanotubes and their use as catalyst support, Catal. Commun. 109 (2018) 65–70, https://doi.org/10.1016/j.catcom.2018.02.024.

[12] J.-J. Fan, Y.-J. Fan, R.-X. Wang, S. Xiang, H.-G. Tang, S.-G. Sun, A novel strategy for the synthesis of sulfur-doped carbon nanotubes as a highly efficient Pt catalyst support toward the methanol oxidation reaction, J. Mater. Chem.A 5 (2017) 19467–19475, https://doi.org/10.1039/C7TA05102F.

[13] M. Soorholtz, R.J. White, T. Zimmermann, M.-M. Titirici, M. Antonietti, R. Palkovits, F. Schüth, Direct methane oxidation over Pt-modified nitrogen-doped carbons, Chem. Commun. 49 (2013) 240–242, https://doi.org/10.1039/C2CC36232E.

[14] L.P. Gonçalves, M. Meledina, A. Meledin, D.Y. Petrovykh, J.P. Sousa, O.S.G. Soares, Y.V. Kolen'ko, M.F.R. Pereira, Understanding the importance of N−doping for CNT-supported Ni catalysts for CO2 methanation, Carbon 195 (2022) 35–43, https://doi.org/10.1016/j.carbon.2022.03.059.

[15] R. Gao, L. Pan, H. Wang, X. Zhang, L. Wang, J.-J. Zou, Ultradispersed nickel phosphide on phosphorus-doped carbon with tailored d-band center for efficient and chemoselective hydrogenation of nitroarenes, ACS Catal. 8 (2018) 8420–8429, https://doi.org/10.1021/acscatal.8b02091.

[16] R. Arrigo, M.E. Schuster, Z. Xie, Y. Yi, G. Wowsnick, L.L. Sun, K.E. Hermann, M. Friedrich, P. Kast, M. Hävecker, A. Knop-Gericke, R. Schlögl, Nature of the N–Pd interaction in nitrogen-doped carbon nanotube catalysts, ACS Catal. 5 (2015) 2740–2753, https://doi.org/10.1021/acscatal.5b00094.

[17] J. Melke, B. Peter, A. Habereder, J. Ziegler, C. Fasel, A. Nefedov, H. Sezen, C. Wöll, H. Ehrenberg, C. Roth, Metal-support interactions of platinum nanoparticles decorated N-doped carbon nanofibers for the oxygen reduction reaction, ACS Appl. Mater. Interfaces 8 (2016) 82–90, https://doi.org/10.1021/acsami.5b06225.

[18] C. Tang, L. Chen, H. Li, L. Li, Y. Jiao, Y. Zheng, H. Xu, K. Davey, S.-Z. Qiao, Tailoring acidic oxygen reduction selectivity on single-atom catalysts via modification of first and second coordination spheres, J. Am. Chem. Soc. 143 (2021) 7819–7827, https://doi.org/10.1021/jacs.1c03135.

[19] J. Zhang, Y. Zhao, C. Chen, Y.-C. Huang, C.-L. Dong, C.-J. Chen, R.-S. Liu, C. Wang, K. Yan, Y. Li, G. Wang, Tuning the coordination environment in single-atom

catalysts to achieve highly efficient oxygen reduction reactions, J. Am. Chem. Soc. 141 (2019) 20118–20126, https://doi.org/10.1021/jacs.9b09352.
[20] W. Wang, G. Yang, Q. Wang, Y. Cao, H. Wang, H. Yu, Modifying carbon nanotubes supported palladium nanoparticles via regulating the electronic metal–carbon interaction for phenol hydrogenation, Chem. Eng. J. 436 (2022), 131758, https://doi.org/10.1016/j.cej.2021.131758.
[21] Q.-Q. Yan, P. Yin, H.-W. Liang, Engineering the electronic interaction between metals and carbon supports for oxygen/hydrogen electrocatalysis, ACS Mater. Lett. 3 (2021) 1197–1212, https://doi.org/10.1021/acsmaterialslett.1c00266.
[22] Y. Chen, R. Gao, S. Ji, H. Li, K. Tang, P. Jiang, H. Hu, Z. Zhang, H. Hao, Q. Qu, X. Liang, W. Chen, J. Dong, D. Wang, Y. Li, Atomic-level modulation of electronic density at cobalt single-atom sites derived from metal-organic frameworks: enhanced oxygen reduction performance, Angew. Chem. Int. Ed. 60 (2021) 3212–3221, https://doi.org/10.1002/anie.202012798.
[23] A.C. Dassanayake, A.A. Gonçalves, J. Fox, M. Jaroniec, One-pot synthesis of activated porous graphitic carbon spheres with cobalt nanoparticles, Colloids Surf., A 582 (2019), 123884, https://doi.org/10.1016/j.colsurfa.2019.123884.
[24] H. Fei, J. Dong, M.J. Arellano-Jiménez, G. Ye, N. Dong Kim, E.L.G. Samuel, Z. Peng, Z. Zhu, F. Qin, J. Bao, M.J. Yacaman, P.M. Ajayan, D. Chen, J.M. Tour, Atomic cobalt on nitrogen-doped graphene for hydrogen generation, Nat. Commun. 6 (2015) 8668, https://doi.org/10.1038/ncomms9668.
[25] C. Rivera-Cárcamo, P. Serp, Single atom catalysts on carbon-based materials, ChemCatChem 10 (2018) 5058–5091, https://doi.org/10.1002/cctc.201801174.
[26] S. Pylypenko, A. Borisevich, K.L. More, A.R. Corpuz, T. Holme, A.A. Dameron, T. S. Olson, H.N. Dinh, T. Gennett, R. O'Hayre, Nitrogen: unraveling the secret to stable carbon-supported Pt-alloy electrocatalysts, Energy Environ. Sci. 6 (2013) 2957, https://doi.org/10.1039/C3EE40189H.
[27] D. Higgins, M.A. Hoque, M.H. Seo, R. Wang, F. Hassan, J.-Y. Choi, M. Pritzker, A. Yu, J. Zhang, Z. Chen, Development and simulation of sulfur-doped graphene supported platinum with exemplary stability and activity towards oxygen reduction, Adv. Funct. Mater. 24 (2014) 4325–4336, https://doi.org/10.1002/adfm.201400161.
[28] Z. Li, Q. Gao, H. Zhang, W. Tian, Y. Tan, W. Qian, Z. Liu, Low content Pt nanoparticles anchored on N-doped reduced graphene oxide with high and stable electrocatalytic activity for oxygen reduction reaction, Sci. Rep. 7 (2017), 43352, https://doi.org/10.1038/srep43352.
[29] A.R. Akbashev, Electrocatalysis goes nuts, ACS Catal. 12 (2022) 4296–4301, https://doi.org/10.1021/acscatal.2c00123.
[30] I.C. Gerber, P. Serp, A theory/experience description of support effects in carbon-supported catalysts, Chem. Rev. 120 (2020) 1250–1349, https://doi.org/10.1021/acs.chemrev.9b00209.
[31] R.G. Rao, R. Blume, T.W. Hansen, E. Fuentes, K. Dreyer, S. Moldovan, O. Ersen, D. D. Hibbitts, Y.J. Chabal, R. Schlögl, J.-P. Tessonnier, Interfacial charge distributions in carbon-supported palladium catalysts, Nat. Commun. 8 (2017) 340, https://doi.org/10.1038/s41467-017-00421-x.
[32] F. Rodriguez-Reinoso, The role of carbon materials in heterogeneous catalysis, Carbon 36 (1998) 159–175, https://doi.org/10.1016/S0008-6223(97)00173-5.
[33] H. Wang, Y. Shao, S. Mei, Y. Lu, M. Zhang, J.-K. Sun, K. Matyjaszewski, M. Antonietti, J. Yuan, Polymer-derived heteroatom-doped porous carbon materials, Chem. Rev. 120 (2020) 9363–9419, https://doi.org/10.1021/acs.chemrev.0c00080.
[34] S.A. Nicolae, H. Au, P. Modugno, H. Luo, A.E. Szego, M. Qiao, L. Li, W. Yin, H. J. Heeres, N. Berge, M.-M. Titirici, Recent advances in hydrothermal carbonisation: from tailored carbon materials and biochemicals to applications and bioenergy, Green Chem. 22 (2020) 4747–4800, https://doi.org/10.1039/D0GC00998A.
[35] Y. Cao, H. Yu, J. Tan, F. Peng, H. Wang, J. Li, W. Zheng, N.-B. Wong, Nitrogen-, phosphorous- and boron-doped carbon nanotubes as catalysts for the aerobic oxidation of cyclohexane, Carbon 57 (2013) 433–442, https://doi.org/10.1016/j.carbon.2013.02.016.
[36] N.F. Sylla, N.M. Ndiaye, B.D. Ngom, B.K. Mutuma, D. Momodu, M. Chaker, N. Manyala, Ex-situ nitrogen-doped porous carbons as electrode materials for high performance supercapacitor, J. Colloid Interface Sci. 569 (2020) 332–345, https://doi.org/10.1016/j.jcis.2020.02.061.
[37] J. Bedia, J.M. Rosas, J. Márquez, J. Rodríguez-Mirasol, T. Cordero, Preparation and characterization of carbon based acid catalysts for the dehydration of 2-propanol, Carbon 47 (2009) 286–294, https://doi.org/10.1016/j.carbon.2008.10.008.
[38] G. Hasegawa, T. Deguchi, K. Kanamori, Y. Kobayashi, H. Kageyama, T. Abe, K. Nakanishi, High-level doping of nitrogen, phosphorus, and sulfur into activated carbon monoliths and their electrochemical capacitances, Chem. Mater. 27 (2015) 4703–4712, https://doi.org/10.1021/acs.chemmater.5b01349.
[39] K. Friedel Ortega, R. Arrigo, B. Frank, R. Schlögl, A. Trunschke, Acid–base properties of N-doped carbon nanotubes, Chem. Mater. 28 (2016) 6826–6839, https://doi.org/10.1021/acs.chemmater.6b01594.
[40] M. Seredych, T.J. Bandosz, Removal of dibenzothiophenes from model diesel fuel on sulfur rich activated carbons, Appl. Catal., B 106 (2011) 133–141, https://doi.org/10.1016/j.apcatb.2011.05.016.
[41] J.C. Meier, C. Galeano, I. Katsounaros, J. Witte, H.J. Bongard, A.A. Topalov, C. Baldizzone, S. Mezzavilla, F. Schüth, K.J.J. Mayrhofer, Design criteria for stable Pt/C fuel cell catalysts, Beilstein J. Nanotechnol. 5 (2014) 44–67, https://doi.org/10.3762/bjnano.5.5.
[42] J. Speder, A. Zana, I. Spanos, J.J. Kirkensgaard, K. Mortensen, M. Hanzlik, M. Arenz, Comparative degradation study of carbon supported proton exchange membrane fuel cell electrocatalysts – the influence of the platinum to carbon ratio on the degradation rate, J. Power Sources 261 (2014) 14–22, https://doi.org/10.1016/j.jpowsour.2014.03.039.
[43] Z. Yu, D. Chen, B. Tøtdal, A. Holmen, Effect of support and reactant on the yield and structure of carbon growth by chemical vapor deposition, J. Phys. Chem. B 109 (2005) 6096–6102, https://doi.org/10.1021/jp0449760.
[44] L.D. Rampino, F.F. Nord, Preparation of palladium and platinum synthetic high polymer catalysts and the relationship between particle size and rate of hydrogenation, J. Am. Chem. Soc. 63 (1941) 2745–2749, https://doi.org/10.1021/ja01855a070.
[45] A. Ohma, K. Shinohara, A. Iiyama, T. Yoshida, A. Daimaru, Membrane and catalyst performance targets for automotive fuel cells by FCCJ membrane, catalyst, MEA WG, ECS Trans. 41 (2011) 775–784, https://doi.org/10.1149/1.3635611.
[46] K. Mayrhofer, D. Strmcnik, B.B. Blizanac, V. Stamenkovic, M. Arenz, N. M. Markovic, Measurement of oxygen reduction activities via the rotating disc electrode method: from Pt model surfaces to carbon-supported high surface area catalysts, Electrochim. Acta 53 (2008) 3181–3188, https://doi.org/10.1016/j.electacta.2007.11.057.
[47] P. Mallet-Ladeira, P. Puech, C. Toulouse, M. Cazayous, N. Ratel-Ramond, P. Weisbecker, G.L. Vignoles, M. Monthioux, A Raman study to obtain crystallite size of carbon materials, Carbon 80 (2014) 629–639, https://doi.org/10.1016/j.carbon.2014.09.006.
[48] J.-R. Cao, M.H. Back, Kinetics of the reaction of hydrogen with thin films of carbon, Carbon 20 (1982) 505–512, https://doi.org/10.1016/0008-6223(82)90087-2.
[49] P.L. Walker, F. Rusinko, L.G. Austin, Gas reactions of carbon, Adv. Catal. 11 (1959) 133–221, https://doi.org/10.1016/S0360-0564(08)60418-6.
[50] B. Xiao, J.P. Boudou, K.M. Thomas, Reactions of nitrogen and oxygen surface groups in nanoporous carbons under inert and reducing atmospheres, Langmuir 21 (2005) 3400–3409, https://doi.org/10.1021/la0472495.
[51] R. Jansen, H. van Bekkum, Amination and ammoxidation of activated carbons, Carbon 32 (1994) 1507–1516, https://doi.org/10.1016/0008-6223(94)90146-5.
[52] E.A. Arkhipova, A.S. Ivanov, N.E. Strokova, S.A. Chernyak, A.V. Shumyantsev, K. I. Maslakov, S.V. Savilov, V.V. Lunin, Structural evolution of nitrogen-doped carbon nanotubes, Carbon 125 (2017) 20–31, https://doi.org/10.1016/j.carbon.2017.09.013.
[53] K. Fujisawa, T. Tojo, H. Muramatsu, A.L. Elías, S.M. Vega-Díaz, F. Tristán-López, J. H. Kim, T. Hayashi, Y.A. Kim, M. Endo, M. Terrones, Enhanced electrical conductivities of N-doped carbon nanotubes by controlled heat treatment, Nanoscale 3 (2011) 4359–4364, https://doi.org/10.1039/C1NR10717H.
[54] M. Seredych, T.J. Bandosz, S-doped micro/mesoporous carbon–graphene composites as efficient supercapacitors in alkaline media, J. Mater. Chem.A 1 (2013), 11717, https://doi.org/10.1039/C3TA12252B.
[55] M. Seredych, J. Jagiello, T.J. Bandosz, Complexity of CO2 adsorption on nanoporous sulfur-doped carbons – is surface chemistry an important factor? Carbon 74 (2014) 207–217, https://doi.org/10.1016/j.carbon.2014.03.024.
[56] H.T. Gomes, S.M. Miranda, M.J. Sampaio, A.M. Silva, J.L. Faria, Activated carbons treated with sulphuric acid, Catal. Today 151 (2010) 153–158, https://doi.org/10.1016/j.cattod.2010.01.017.
[57] M. Seredych, K. Singh, T.J. Bandosz, Insight into the capacitive performance of sulfur-doped nanoporous carbons modified by addition of graphene phase, Electroanalysis 26 (2014) 109–120, https://doi.org/10.1002/elan.201300161.
[58] A.P. Terzyk, Further insights into the role of carbon surface functionalities in the mechanism of phenol adsorption, J. Colloid Interface Sci. 268 (2003) 301–329, https://doi.org/10.1016/S0021-9797(03)00690-8.
[59] W.E. Morgan, W.J. Stec, R.G. Albridge, J.R. van Wazer, pi, -Bond feedback interpreted from the binding energy of the "2p" electrons of phosphorus, Inorg. Chem. 10 (1971) 926–930, https://doi.org/10.1021/ic50099a013.
[60] J. Wu, C. Jin, Z. Yang, J. Tian, R. Yang, Synthesis of phosphorus-doped carbon hollow spheres as efficient metal-free electrocatalysts for oxygen reduction, Carbon 82 (2015) 562–571, https://doi.org/10.1016/j.carbon.2014.11.008.
[61] J.F. Moulder, W.F. Stickle, P.E. Sobol, K.D. Bomben, Handbook of X-Ray Photoelectron Spectroscopy: A Reference Book of Standard Spectra for Identification and Interpretation of XPS Data, Perkin-Elmer Corporation, Eden Prairie, Minnesota, US, 1993.
[62] L.R. Radović, P.L. Walker, R.G. Jenkins, Importance of carbon active sites in the gasification of coal chars, Fuel 62 (1983) 849–856, https://doi.org/10.1016/0016-2361(83)90041-8.
[63] P. Ehrburger, F. Louys, J. Lahaye, The concept of active sites applied to the study of carbon reactivity, Carbon 27 (1989) 389–393, https://doi.org/10.1016/0008-6223(89)90071-7.
[64] N.R. Laine, F.J. Vastola, P.L. Walker, The importance of active surface area in the carbon-oxygen reaction, J. Phys. Chem. 67 (1963) 2030–2034, https://doi.org/10.1021/j100804a016.
[65] S. Zhang, X. Yuan, H. Wang, W. Merida, H. Zhu, J. Shen, S. Wu, J. Zhang, A review of accelerated stress tests of MEA durability in PEM fuel cells, Int. J. Hydrogen Energy 34 (2009) 388–404, https://doi.org/10.1016/j.ijhydene.2008.10.012.
[66] N. Linse, L. Gubler, G.G. Scherer, A. Wokaun, The effect of platinum on carbon corrosion behavior in polymer electrolyte fuel cells, Electrochim, Acta 56 (2011) 7541–7549, https://doi.org/10.1016/j.electacta.2011.06.093.
[67] M.A. Hoque, F.M. Hassan, A.M. Jauhar, G. Jiang, M. Pritzker, J.-Y. Choi, S. Knights, S. Ye, Z. Chen, Web-like 3D architecture of Pt nanowires and sulfur-doped carbon nanotube with superior electrocatalytic performance, ACS Sustainable Chem. Eng. 6 (2018) 93–98, https://doi.org/10.1021/acssuschemeng.7b03580.
[68] C. Galeano, J.C. Meier, M. Soorholtz, H. Bongard, C. Baldizzone, K.J.J. Mayrhofer, F. Schüth, Nitrogen-doped hollow carbon spheres as a support for platinum-based electrocatalysts, ACS Catal. 4 (2014) 3856–3868, https://doi.org/10.1021/cs5003492.